Engineering 65 (2026) 255–268

Contents lists available at ScienceDirect

Engineering

journal homepage: www.elsevier.com/locate/eng

Research
Medical Engineering—Article

Urchin-Shaped COFs Empower Dual-Mode Sensor Integrating Multiple Signal Amplification for Ultrasensitive miRNA-21 Detection

Xinxue Zhang [a], Pengfei Dong [a], Youfa Wang [a], Shuang Wu [a], Lili Zhang [a], Jie Han [a], Geoffrey I. N. Waterhouse [b], Quancai Sun [c], Jing Huang [a,*], Jin Wang [a,d,*]

[a] Key Laboratory of Environmental Medicine and Engineering (MOE) & Department of Nutrition and Food Hygiene, School of Public Health, Southeast University, Nanjing 210009, China
[b] School of Chemical Sciences, The University of Auckland, Auckland 1142, New Zealand
[c] Faculty of Medicine, Macau University of Science and Technology, Macao 999078, China
[d] Department of Bioresource Engineering, Faculty of Agricultural and Environmental Sciences, McGill University, Sainte-Anne-de-Bellevue, QC H9X 3V9, Canada

ARTICLE INFO

Article history:
Received 5 December 2025
Revised 16 January 2026
Accepted 12 March 2026
Available online 18 March 2026

Keywords:
Multiple signal amplification
Dual-mode sensor
miRNA-21 detection
Urchin-shaped covalent organic framework

ABSTRACT

MicroRNAs (miRNAs) are promising biomarkers for cancer, offering a minimally invasive approach for liquid biopsy. However, their low abundance in clinical samples poses a major challenge for detection sensitivity and analytical reliability. Herein, this study reports a fluorescence–electrochemical dual-mode sensor that integrates multiple signal amplification strategies for the ultrasensitive detection of miRNA-21. MXene–gold nanoparticle (AuNP) composite were first modified on the electrode surface to enable efficient probe loading and enhanced electron transfer to amplify signal. The urchin-shaped covalent organic frameworks (COFs) facilitated more efficient methylene blue loading, with the unique structure further enhancing signal response. Combined with the miRNA-21 triggered entropy-driven catalysis (EDC)–DNA catalysis (DNAzyme) cascade amplification, the sensor realized a multi-level synergistic signal enhancement, demonstrating remarkable sensitivity. Notably, the urchin-shaped COFs served dual roles as both fluorescent reporters and nanocarriers, facilitating dual-mode signal readout. Under optimized conditions, the sensor exhibited a linear response to miRNA-21 in the range of 1–10^5 fmol·L^{-1}, with detection limits of 0.285 and 0.342 fmol·L^{-1} for the electrochemical and fluorescence modes, respectively. The platform enabled accurate detection of miRNA-21 in human serum and cancer cells. It provides a viable pathway for early cancer diagnosis with sensitivity and reliability.

© 2026 THE AUTHORS. Published by Elsevier LTD on behalf of Chinese Academy of Engineering and Higher Education Press Limited Company. This is an open access article under the CC BY-NC-ND license (http://creativecommons.org/licenses/by-nc-nd/4.0/).

1. Introduction

Early diagnosis of cancer is critical for guiding effective treatment and improving patient survival. Conventional invasive techniques, such as biopsy and endoscopy, are widely used in clinical practice. However, their complexity and associated risks limit their applicability for continuous monitoring of early lesions [1]. Liquid biopsy has emerged as a non-invasive, efficient, and real-time alternative. It enables the capture of circulating molecular biomarkers before visible histopathological changes occur, thereby offering a more sensitive early warning signal [2]. Among these biomarkers, microRNAs (miRNAs) have attracted considerable attention. They are endogenous, non-coding RNAs approximately 19–25 nucleotides in length. miRNAs play a key role in regulating gene expression and are closely linked to the development of various cancers. In particular, miRNA-21 is a representative oncogenic miRNA that is consistently overexpressed in multiple malignancies. It has emerged as a reliable biomarker for early diagnosis [3]. Therefore, developing a simple, accurate, and highly sensitive miRNA-21 detection method is essential for advancing early diagnostic capabilities in cancer.

Currently, several established analytical techniques are available for detecting miRNA-21, including quantitative real-time fluorescent polymerase chain reaction (qRT-PCR), northern blot, and next-generation sequencing. However, these techniques generally involve high costs, lengthy processing times, and reliance on specialized equipment, limiting their widespread application [4]. With the rapid progress of biosensing technologies, various new platforms, such as electrochemical, fluorescent, and colorimetric

* Corresponding authors.
E-mail addresses: huangjing@seu.edu.cn (J. Huang), jin.wang6@mail.mcgill.ca (J. Wang).

https://doi.org/10.1016/j.eng.2026.03.007
2095-8099/© 2026 THE AUTHORS. Published by Elsevier LTD on behalf of Chinese Academy of Engineering and Higher Education Press Limited Company.
This is an open access article under the CC BY-NC-ND license (http://creativecommons.org/licenses/by-nc-nd/4.0/).

sensors have emerged, accelerating the evolution of miRNA-21 detection toward faster, more portable, and more affordable approaches. For example, Dong et al. [5] constructed fluorescent signal probes by synthesizing gold nanoparticles (AuNPs) and silver nanoclusters, achieving femtomolar-level quantitative detection of miRNA-21. In another study, Yang et al. [6] designed a dissipative DNA network for electrochemical detection of miRNA-21. This design enabled self-resetting capability and significantly improved both reusability and sensitivity. Notably, both approaches rely on a single signal output channel. Such systems remain vulnerable to environmental interference, which can lead to signal error and compromised reliability [7]. To address this limitation, increasing attention has been directed toward dual-mode sensing strategies. These platforms integrate two independent yet complementary signal transduction mechanisms [8,9]. For example, Shi et al. [10] developed an electrochemical–colorimetric dual-mode sensor based on DNA nanorings, AuNPs, and graphdiyne for the specific detection of miRNA-21. Through complementary signal verification and self-calibration, this system effectively improved interference resistance and analytical accuracy. Consequently, constructing dual-mode sensing platform with self-calibration capability has become a highly promising and necessary development direction for achieving reliable and precise miRNA detection in complex biological environments.

The extremely low abundance of miRNA-21 in body fluids poses a major challenge for sensor sensitivity. To address this, two main strategies are typically employed: integrating functionalized nanomaterials to enhance target capture and incorporating signal amplification mechanisms to boost response intensity [11,12]. Among them, non-enzymatic signal amplification strategy have attracted widespread attention due to their operational simplicity and stability. These approaches applied the programmability of DNA to construct isothermal amplification via strand hybridization and displacement [13]. Representative non-enzymatic amplification methods have been widely used for highly sensitive miRNA detection, such as hybridization chain reaction (HCR), catalytic hairpin assembly (CHA), DNA catalysis (DNAzyme), and entropy-driven catalysis (EDC) [14–18]. It is worth noting that, due to the high programmability of DNA, various multi-module cascade amplification strategies have been developed, such as CHA–DNAzyme, CHA–HCR, and EDC–DNAzyme. These systems employ upstream reaction products as triggers to activate downstream amplification modules, enabling multi-stage amplification with markedly enhanced sensitivity [19–21]. Specifically, the EDC–DNAzyme strategy combines the low background of EDC with the highly efficient catalytic properties of DNAzyme, achieving efficient and specific miRNA detection without reliance on proteases, demonstrating unique application potential.

With advances in nanotechnology, multifunctional materials also play a crucial role in improving sensor performance. MXene, a novel two-dimensional nanomaterial, is typically constructed by selectively etching the A layer from MAX phase precursors, which consist of the transition metal (M), the main group element (A), and carbon and/or nitrogen (X) [22,23]. Owing to its high metallic conductivity, large surface area, and layered structure with abundant active sites, MXene has attracted considerable attention in sensing platform [24,25]. To further enhance sensor performance, noble metal nanoparticles, particularly AuNPs, have been integrated into MXene to construct MXene–AuNPs. These composite materials markedly enhance electrochemical responsiveness and target recognition, making them ideal candidates for the development of high-performance electrochemical sensors [26]. In parallel, covalent organic frameworks (COFs), a class of ordered porous crystals linked by strong covalent bonds, have also attracted significant attention due to their high surface area, tunable pores, and exceptional stability [27]. The unique porous structure not only enhances the interaction between target molecules and probes, but also efficiently enriches electroactive molecules through adsorption or electrostatic interactions. This significantly enhances the local current density, providing COFs with a distinct advantage as carrier in developing highly sensitive electrochemical sensors [28]. Meanwhile, the programmable organic frameworks and π-conjugated systems endow some COFs with excellent fluorescence properties. By incorporating optical functional groups, COFs can generate fluorescence changes upon target recognition, demonstrating potential as fluorescent probes [29]. This dual functionality of COFs provides new avenues for designing multi-mode sensor platforms, further improving detection accuracy and anti-interference capabilities.

Inspired by these advantages, this study rationally designed a fluorescence–electrochemical dual-mode sensor with the multiple signal amplification strategy for highly sensitive detection of miRNA-21. First, we synthesized MXene–AuNPs composites and modified them onto the electrode. These materials improve both electrical conductivity and probe loading capacity, providing initial signal amplification. Next, we constructed urchin-shaped COFs with hierarchical porous structures. These COFs serve as an efficient carrier for loading methylene blue (MB), an electrochemical signal molecule. This design enhances the current response and further amplifies the signal. Importantly, the urchin-shaped COFs also exhibit intrinsic fluorescence, directly generating an optical readout. This dual functionality establishes a solid material foundation for constructing a fluorescence–electrochemical sensor. To achieve multilevel signal amplification, we introduced an EDC–DNAzyme cascade strategy. Even trace amounts of miRNA-21 can trigger this cascade, producing a marked increase in fluorescence signal along with a steep decrease in electrochemical signal. Together, these dynamic changes not only further enhanced the overall sensitivity of sensor, but also ensure reliable detection through the complementarity and self-correction of fluorescence and electrochemical signals in complex body fluid, providing powerful technical support for early disease diagnosis.

2. Experimental section

2.1. Reagents and apparatus

The related information was presented in Sections S1.1 and S1.2 in Appendix A.

2.2. Synthesis of MXene and MXene–AuNPs

Based on previously reported approaches, the preparation method for MXene–AuNPs was suitably modified [24]. First, MXene was synthesized through chemical etching. Briefly, 500 mg of titanium aluminium carbide (Ti_3AlC_2) powder was gradually added to 20 mL of 40% hydrofluoric acid (HF) and stirred at 35 °C for 36 h. The precipitate was repeatedly washed with deionized water until the supernatant of the final centrifugation reached a pH above 6, after which the solid was collected and freeze-dried. For AuNPs loading, 40 mg of the prepared MXene was ultrasonically dispersed in 40 mL of ultrapure water to form a uniform suspension. Then, 4 mL of a 1% chloroauric acid ($HAuCl_4{\cdot}3H_2O$) solution was slowly introduced, followed by stirring at 35 °C for 20 min. The final product was collected by centrifugation and freeze-dried to obtain MXene–AuNPs.

2.3. Preparation of urchin-shaped COFs

To prepare the urchin-shaped COFs, 28.1 mg of 1,3,5-tri(4-aminophenyl)benzene (TAPB) and 23.3 mg of

2,5-dimethoxybenzene-1,4-dicarboxaldehyde (DMTA) were dissolved in 10 mL acetonitrile under ultrasonication until clear. Then, 2.6 mL of 12 mol·L^{-1} acetic acid was added at 1000 r·min^{-1} and stirred for 1 min, followed by standing at room temperature (RT) for 48 h. The product was collected by centrifugation, washed several times with tetrahydrofuran and ethanol, and vacuum-dried at 60 °C for 12 h.

2.4. Preparation of DNA strand H5-functionalized COFs (H5–COFs) probe

Prior to use, H5 (10 μmol·L^{-1}) was heated at 95 °C for 5 min and slowly cooled to RT to promote the formation of the hairpin structure. Subsequently, 100 μL of 20 mg·mL^{-1} EDC/*N*-hydroxysuccinimide (NHS) and 5 mmol·L^{-1} Tris(2-carboxyethyl) phosphine hydrochloride were added to the H5 solution. The activated H5 was combined with 100 μL of urchin-shaped COFs solution and incubated at 37 °C for 2 h. The mixture was centrifuged at 8000 r·min^{-1} for 10 min to remove unreacted DNA, and the precipitate was washed several times with phosphate-buffered saline (PBS). The final product (H5–COFs) was dispersed in ultrapure water and stored at 4 °C for further use.

2.5. EDC amplification system

First, DNA strands H1–H4 (1 μmol·L^{-1} each) were first heated at 95 °C for 5 min and slowly cooled to RT. H1, H2, and H3 were mixed and incubated at 37°C for 2 h to form a stable three-stranded complex. Subsequently, varying concentrations of miRNA-21 were introduced to initiate the reaction. Fuel strand H4 (5 μL) was then added and the mixture was further incubated at 37 °C for 1 h. The final amplification system consisted of H1–H4 complexes together with unbound H2, H3, and miRNA-21, where miRNA-21 re-entered the cycle to continuously drive the amplification process.

2.6. Construction of the dual-mode sensor

The glassy carbon electrode (GCE) was polished using alumina slurry and rinsed with ultrapure water to remove impurities. The GCE/MXene–AuNPs were prepared by dropping 5 μL of MXene–AuNPs solution (1 mg·mL^{-1}) onto the electrode surface and incubating at 37 °C for 45 min. Subsequently, 5 μL of H5–COFs was immobilized onto the electrode surface via Au–S bonding to obtain GCE/MXene–AuNPs/H5–COFs. To block nonspecific binding sites, the electrode was treated with 0.1 mmol·L^{-1} 6-mercapto-1-hexanol (MCH) for 40 min. After each modification step, the electrode was rinsed three times with PBS to remove unbound materials. Next, 5 μL of the EDC reaction product and 5 μL of 20 mmol·L^{-1} Pb^{2+} were added to the electrode and incubated at 37 °C for 90 min. Following the reaction, the cleaved H5–COFs fragments were collected in 50% ethanol for fluorescence analysis. Finally, 5 μL MB (2 mmol·L^{-1}) was added to the electrode plate and incubate for 75 min. After rinsing, differential pulse voltammetry (DPV) was collected to record the electrochemical signal.

2.7. Real sample analysis

HeLa (cervical cancer), MCF-7 (breast cancer), and HCT116 (colorectal cancer) cells were cultured in medium supplemented with 10% fetal bovine serum and penicillin–streptomycin, and were maintained in Dulbecco's Modified Eagle Medium (DMEM). All cells were incubated at 37 °C in a humidified atmosphere with 5% CO_2. To obtain cell lysates, cells grown to the desired density were first rinsed with PBS and resuspended in 500 μL of lysis buffer. Total RNA was then extracted from the three cell types using the Trizol method and stored at –80 °C until use. Finally, miRNA-21 levels in these cells were assessed using both the constructed sensor and qRT-PCR.

3. Results and discussion

3.1. Principle of dual-mode sensor detection for miRNA-21

Fig. 1 illustrates the principle of the fluorescence–electrochemical dual-mode sensor based on the multi-signal amplification strategy for miRNA-21 detection. The sensor construction began with the preparation of layered MXene by chemical etching, followed by the *in situ* reduction of $HAuCl_4$ to uniformly anchor AuNPs onto its surface, thereby forming MXene–AuNPs nanocomposites modified on the electrode. This substrate provided both efficient electron transport and abundant active sites, establishing a platform for subsequent electrochemical reactions, achieving preliminary signal amplification in the sensor (Fig. 1(a)). In parallel, urchin-shaped COFs were synthesized at RT through Schiff base condensation between TAPB and DMTA, with acetic acid content carefully tuned to control the morphology. These COFs exhibited strong intrinsic fluorescence and, more importantly, their porous frameworks enabled efficient loading of the signal molecule MB. This structural advantage further contributed to signal enhancement. Subsequently, the COFs were covalently coupled with carboxyl-functionalized H5 via amide reaction to form the H5–COFs probe for the sensing platform. This design facilitated the subsequent dual-mode output of fluorescence and electrochemical signals (Fig. 1(b)).

In construction of the dual-mode sensor (Fig. 1(c)), MXene–AuNPs were first immobilized onto the electrode surface. The H5–COFs probe was then anchored through Au–S bonds formed between its terminal thiol groups and the AuNPs. Finally, remaining active sites were blocked with MCH. These H2 strands acted as triggers for the downstream DNAzyme cycle by hybridizing with the recognition domain of H5, which contained an rA cleavage site. This hybridization activated the Pb^{2+}-dependent DNAzyme, enabling cleavage of the H5–COFs probe. Importantly, miRNA-21 was not consumed during this process but re-entered successive cycles, continuously driving the cascade reaction. Through this cyclic triggering–cascade cleavage mechanism, extensive fragmentation of the H5–COFs probe was achieved, resulting in significant signal amplification. On the one hand, the fragmented H5–COFs released into the ethanol solution generated an enhanced fluorescence signal. On the other hand, the reduced amount of H5–COFs available on the electrode surface for MB loading led to a pronounced decrease in the electrochemical signal.

This fluorescence–electrochemical sensor detects miRNA-21 with high sensitivity and accuracy. The design combines three functional elements including MXene–AuNPs for signal transduction, urchin-shaped COFs for signal generation, and an EDC–DNAzyme cascade for signal amplification. More importantly, the dual-mode readout provides built-in self-calibration, ensuring reliable measurement of low-abundance miRNA-21 in body fluids.

3.2. Characterization of MXene–AuNPs nanocomposites

The synthesis of MXene–AuNPs was illustrated in Fig. 2(a). First, the aluminum layer of Ti_3AlC_2 was selectively etched using HF, successfully yielding $Ti_3C_2T_x$ MXene with an expanded interlayer spacing. Owing to the surface termination groups (–F, –O, and –OH) on MXene nanosheets, $AuCl_4^-$ could be directly reduced by –OH groups to form AuNPs anchored onto the MXene surface. To investigate the structural characteristics, scanning electron microscopy (SEM) was performed on Ti_3AlC_2, MXene, and MXene–AuNPs, respectively. As shown in Fig. 2(b), Ti_3AlC_2 (MAX phase)

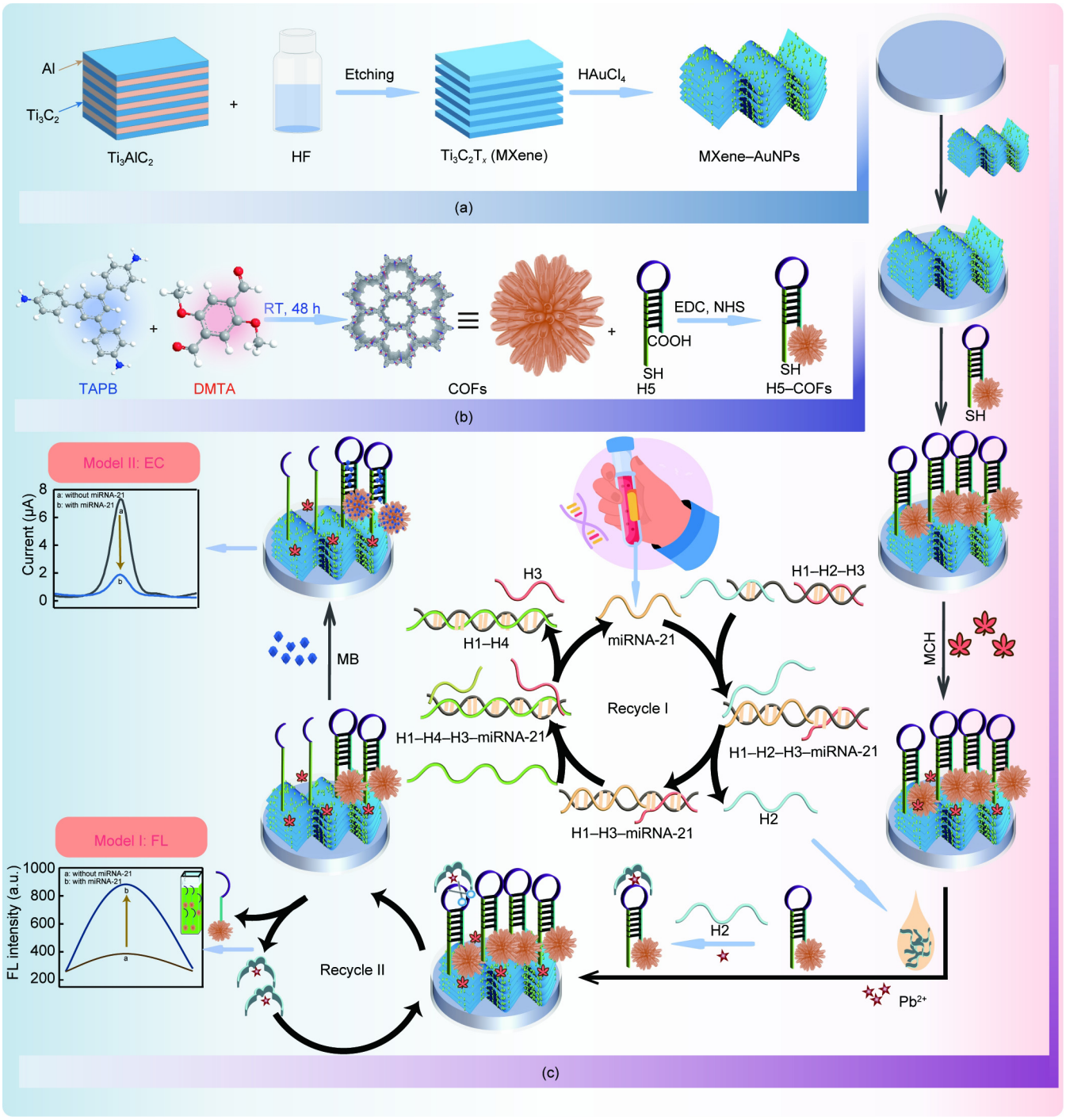


Fig. 1. Principles and construction of the dual-mode sensor based on multiple signal amplification. (a) Synthesis of MXene–AuNPs nanocomposite material. (b) Preparations of urchin-shaped COFs and construction of H5–COFs probe. (c) Design of the fluorescence–electrochemical dual-mode sensor for miRNA-21 detection. EC: electrochemical; FL: fluorescence.

exhibited a typical cubic block-like morphology. After the removal of Al, MXene displayed a graphene-like, accordion-shaped multilayer structure, which was consistent with previous reports [30]. This unique nanostructure provided a larger surface area, substantially enhancing interfacial reaction efficiency. Furthermore, after reduction, Au^{3+} formed uniformly distributed AuNPs on the layered surface of MXene. Elemental mapping confirmed the uniform distribution of Au, Ti, O, and F, validating the compositional homogeneity and structural stability of the MXene–AuNPs. With the superior electron transport capability of MXene and the abundant binding sites contributed by AuNPs, the MXene–AuNPs would make significant contributions in advancing highly sensitive electrochemical detection [31].

The composition and crystal structure of the material were further confirmed by X-ray diffraction (XRD) in Fig. 2(c). The characteristic peaks of Ti_3AlC_2 matched well with the standard reference (PDF#52-0875). After etching, the (104) peak of Ti_3AlC_2 disappeared, while the distinct peaks of MXene at (004), (006), (103), (105), and (110) emerged, indicating complete removal of aluminum and the successful synthesis of multilayer MXene [32].

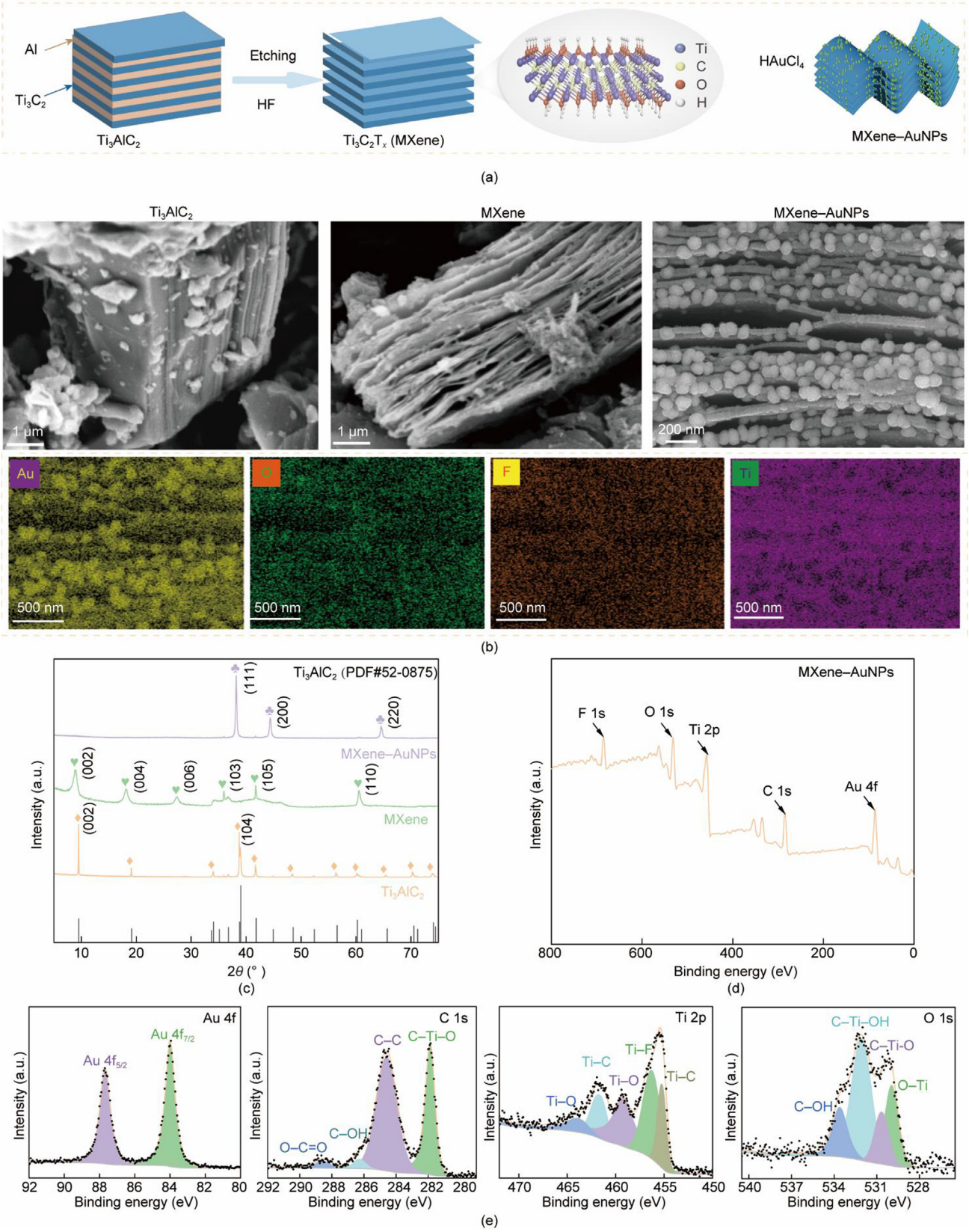


Fig. 2. Characterization of MXene–AuNPs nanocomposite. (a) The synthesis route of MXene–AuNPs. (b) SEM of Ti_3AlC_2, MXene, MXene–AuNPs, and corresponding element distribution in MXene–AuNPs. (c) X-ray diffraction of Ti_3AlC_2, MXene, and MXene–AuNPs. (d) Full-region X-ray photoelectron spectroscopy spectrum of MXene–AuNPs. (e) The high-resolution XPS spectra of Au 4f, C 1s, Ti 2p, and O 1s in MXene–AuNPs.

After *in situ* reduction of $HAuCl_4$, additional peaks appeared at 38.7°, 45.0°, and 65.2°, corresponding to the (111), (200), and (220) planes of face-centered cubic Au. These results collectively confirmed the successful formation of MXene–AuNPs [33]. X-ray photoelectron spectroscopy (XPS) technique was employed to investigate the electronic states and chemical composition. The full XPS spectra (Fig. 2(d)) revealed the presence of F, O, Ti, C, and Au, confirming the successful formation of MXene–AuNPs. As shown in Fig. 2(e), the Au 4f spectrum displayed two peaks at 83.95 and 87.7 eV, corresponding to Au $4f_{7/2}$ and Au $4f_{5/2}$, respectively. The binding energy gap between these two peaks was 3.75 eV, indicating the successful reduction of Au to Au (0) [34]. In C 1s spectrum, four characteristic peaks were observed at 281.85, 284.6, 286.3, and 288.6 eV, corresponding respectively to the C–Ti–O, C–C, C–OH, and O–C=O groups. The Ti 2p spectrum revealed three characteristic Ti chemical states within MXene–AuNPs, namely Ti–O, Ti–C, and Ti–F, with corresponding binding energies of 459.2/464.01 eV, 455.2/461.8 eV, and 456.34 eV. In addition, the O 1s spectrum could be deconvoluted into four peaks at 529.59, 530.7, 532.1, and 533.6 eV. The first three peaks were attributed to O–Ti, C–Ti–O, and C–Ti–OH, respectively, while the 533.6 eV peak corresponded to physically or chemically adsorbed water [35].

3.3. Characterization of the signal probe H5–COFs

The preparation method of the signal probe H5–COFs is shown in Fig. 3(a). Unlike conventional solvothermal synthesis, in this work, TAPB and DMTA were employed as reacting monomers, yielding the uniform COFs through 48 h at RT [36]. Given that the concentration of reducing agent (acetic acid) significantly influences the morphology of COFs, this study successfully synthesized urchin-shaped COFs with stronger adsorption capacity and larger specific surface area [37]. In addition, the abundant amino groups on the urchin-shaped COFs surface allowed H5 to be stably immobilized through the condensation reaction between amino and carboxyl groups, thereby constructing the signal probe [38]. The SEM image reveals that the COFs adopt a distinct urchin-shaped morphology with uniformly protruding surfaces (Fig. 3(b)). Transmission electron microscopy (TEM) image further highlights that its interior exhibits a regular radial branching architecture. This radial structure provides abundant micropores and interconnected channels, facilitating rapid molecular diffusion into the framework and markedly enhancing adsorption performance (Fig. 3(c)). Subsequently, the synthesis of the H5–COFs probe was investigated by energy-dispersive spectroscopy (EDS). The results revealed that the surface of H5–COFs contained four elements, namely C, N, O, and P (Fig. 3(d)). In contrast, the EDS imaging of urchin-shaped COFs displayed only C, N, and O elements (Fig. S1 in Appendix A). This indicated that the single-stranded H5 had successfully attached to the COF surface [39]. Then, the structure of COFs was examined using Fourier transform infrared (FT-IR). As shown in Fig. 3(e), a distinct band at 1592 cm^{-1} corresponding to C=N stretching confirmed the formation of imine linkages through the Schiff-base reaction between the amine groups of TAPB and the aldehyde groups of DMTA. Concurrently, the disappearance of the amino group stretching vibration peaks of TAPB at 3212 and 3355 cm^{-1}, along with the characteristic aldehyde peak of DMTA at 1676 cm^{-1}, further corroborated the formation of imine bonds within the urchin-shaped COFs [40]. Importantly, the crystallinity of the COFs was verified by powder XRD (PXRD). As shown in Fig. 3(f), the urchin-shaped COFs exhibited a strong diffraction peak at 2θ = 2.78°, accompanied by a series of weaker peaks at 2θ = 4.78°, 5.56°, 7.36°, 9.66°, and 25.22°. These corresponded to the (100), (110), (200), (210), (220), and (001) crystal planes, indicating the material possessed excellent crystallinity [41]. Interestingly, theoretical modeling using Materials Studio revealed that the experimental PXRD pattern closely matched the simulated pattern based on the AA stacking model, with fitting parameters of profile residual (R_p) = 3.36% and weighted profile residual (R_{wp}) = 4.87%. The COFs crystallized in the P6/M space group with lattice parameters $a = b$ = 38.05 Å, c = 3.85 Å, $\alpha = \beta$ = 90°, and γ = 120° [42]. Accordingly, the calculated pore diameter of 3.3 nm provided sufficient space to facilitate the diffusion and encapsulation of small dye molecules such as MB (14.5 Å × 9.5 Å × 4.2 Å) within the channels (Fig. 3(g)) [43].

Meanwhile, XPS was further employed to examine the chemical composition and elemental states of the COFs. In the full spectrum, signals at 285, 399, and 534 eV were assigned to C 1s, N 1s, and O 1s, respectively (Fig. 3(h)) [44]. The chemical composition and bonding states of the COFs were further confirmed by deconvolution of the respective elemental peaks (Fig. S2 in Appendix A). In the C 1s region, peaks at 284.8 and 286.5 eV were attributed to C–C and C–O bonds. The N 1s spectrum showed peaks at 398.9 and 399.7 eV, corresponding to C=N and C–N bonds, while the O 1s spectrum exhibited two peaks at 531.8 and 533.6 eV, indicating the presence of C–O and C=O groups within the framework. Furthermore, the fluorescence property of the COFs was investigated, revealing optimal excitation and emission wavelengths of 402 and 515 nm, respectively. In aqueous solution, they appeared pale yellow under natural light, while exhibiting a bright green emission under ultraviolet irradiation (Fig. 3(i)). More significantly, the fluorescence intensity of the COFs remained virtually unchanged over extended storage periods, retaining 96.9% of their initial fluorescence level after ten days (Fig. S3 in Appendix A). In addition, the thermal stability of the urchin-shaped COFs was evaluated using thermogravimetric analysis (TGA) under the N_2 atmosphere. As depicted in the TGA results, they exhibited excellent thermal stability prior to 400 °C, with approximately 3.5% weight loss, primarily attributed to the evaporation of residual water and organic solvents (Fig. S4 in Appendix A) [45]. These findings collectively demonstrated that the urchin-shaped COFs could serve as effective carriers and stable luminescent element for sensor applications. Notably, after modification with DNA, the zeta potential shifted from −28.29 to −40.96 mV (Fig. 3(j)) [46]. This result was consistent with the EDS results, both confirming the effective construction of the H5–COFs probe.

3.4. Construction of fluorescence–electrochemical dual-mode sensor

To validate the successful construction of the dual-mode sensor based on multiple signal amplification, the stepwise assembly of the electrode was first systematically examined using electrochemical impedance spectroscopy (EIS) and cyclic voltammetry (CV). In the Nyquist plots from EIS, the electron transfer resistance (Ret) is reflected by the diameter of the semicircle. As shown in Fig. 4(a), the Ret value of the polished bare GCE was 176.59 Ω (curve i), attributed to the relatively facile electron transfer of $[Fe(CN)_6]^{3-/4-}$ on the unmodified electrode. Following modification with MXene–AuNPs, the resistance decreased to 128.95 Ω owing to the excellent conductivity of the nanocomposite (curve ii). Furthermore, when the H5–COFs probe was anchored to the electrode surface through Au–S bonds, the Ret rose sharply to 474.76 Ω (curve iii). This increase was attributed to the negatively charged phosphate backbone of H5, which repelled the negatively charged $[Fe(CN)_6]^{3-/4-}$ in solution, along with additional steric hindrance from the COFs framework [47]. Subsequently, blocking the remaining active sites with MCH caused a further increase in resistance to 557.74 Ω (curve iv). Notably, when MB molecules were absorbed into the stem-loop structure of H5 and confined within the pores of urchin-shaped COFs, the Ret reached its maximum value of 938.56 Ω due to the poor conductivity of MB (curve v). Finally,

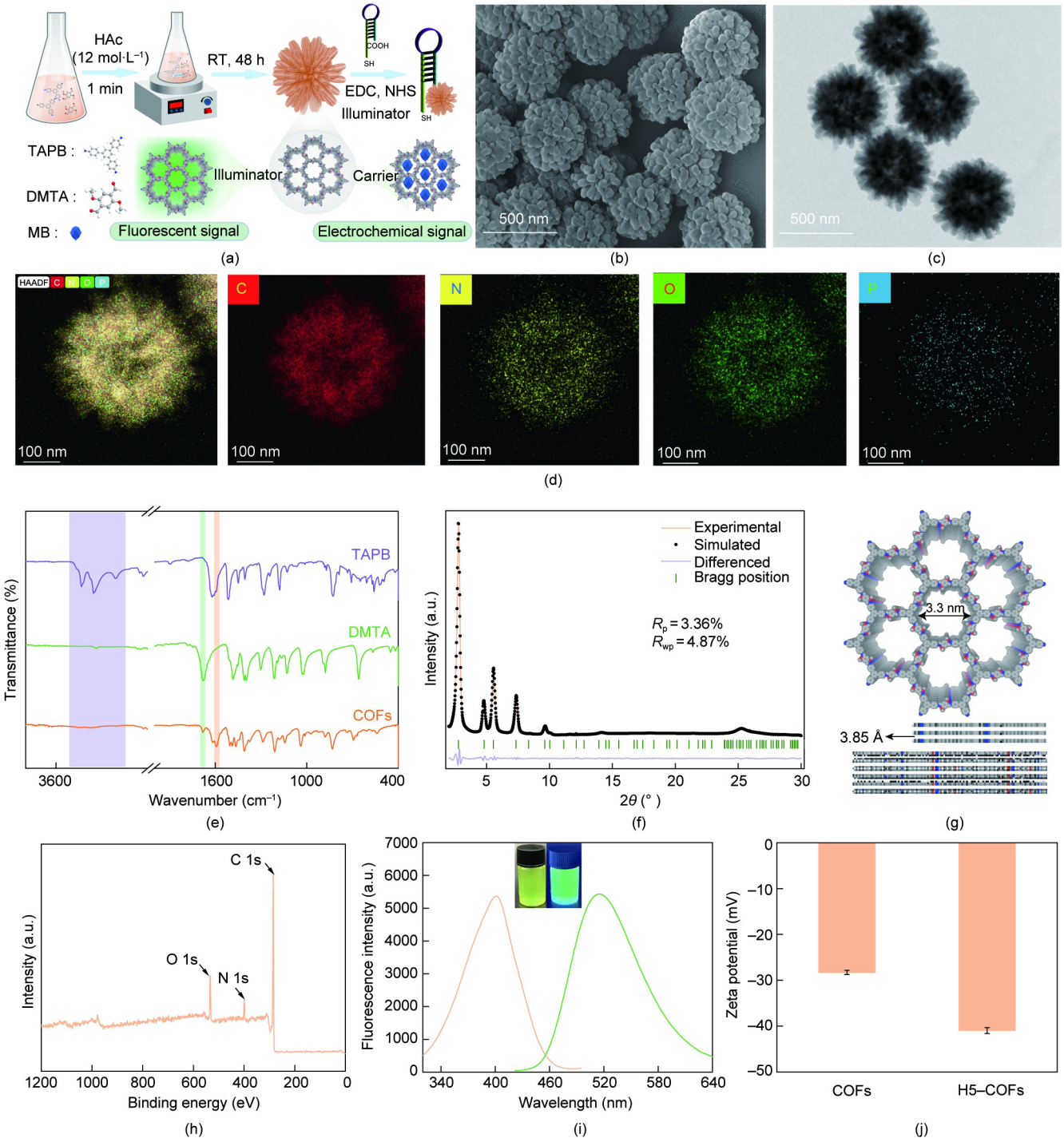


Fig. 3. Construction of H5–COFs signal probe based on urchin-shaped COFs. (a) Synthesis route for H5–COFs signal probe with dual functions as illuminator and carrier. (b) SEM images of the urchin-shaped COFs. (c) TEM images of the H5–COFs. (d) The corresponding EDS elemental mapping images of H5–COFs. (e) FT-IR spectrum of TAPB, DMTA, and the urchin-shaped COFs. (f) PXRD pattern. (g) Eclipsed stacking. (h) High-resolution XPS spectra of urchin-shaped COFs. (i) Excitation and emission spectra of urchin-shaped COFs. The inset shows the photos of the COFs under daylight (left) and ultraviolet light (right). (j) Zeta potential measurements of COFs and H5–COFs.

H2 containing the DNAzyme sequence and the catalyst Pb^{2+} were simultaneously introduced onto the electrode surface, causing the Ret value to decrease to 570.1 Ω (curve vi). This decrease was caused by the Pb^{2+}-activated cleavage of the DNAzyme substrate embedded in H5, which disrupted the stem-loop configuration and released the MB-loaded COFs probes from the electrode surface. The resulting reduction in steric hindrance created more favorable conditions for electron transfer [48,49]. Correspondingly, the CV curves in Fig. 4(b) clearly tracked the same progressive assembly process. The consistency between EIS and CV confirmed the successful construction of the electrochemical sensor. Furthermore, to clarify the origin of signals on the electrodes, different functional materials were individually modified onto the electrode surfaces, and their electrochemical responses were systematically evaluated via DPV (Fig. S5 in Appendix A). As a result, when the electrode was immobilized solely with H5 or H5–COFs, negligible current signals were observed due to the absence of electroactive molecules. In contrast, upon introducing

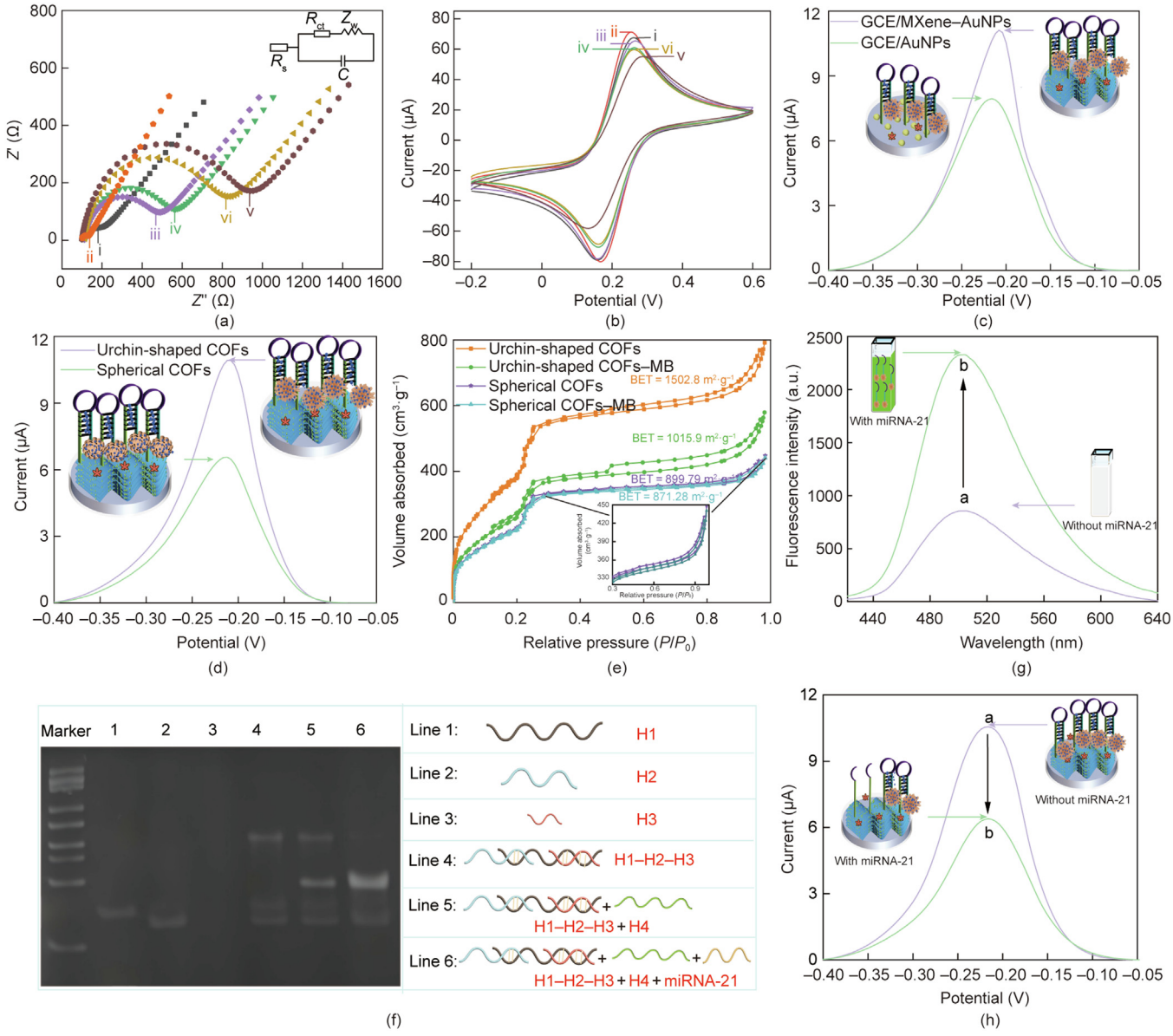


Fig. 4. Construction of the dual-mode sensor for miRNA-21 detection. (a) EIS and (b) CV characterization of electrodes at various steps of modification in a 5 mmol·L^{-1} $[Fe(CN)_6]^{3-/4-}$ solution: i: GCE, ii: GCE/MXene–AuNPs, iii: GCE/MXene–AuNPs/H5–COFs, iv: GCE/MXene–AuNPs/H5–COFs/MCH, v: GCE/MXene–AuNPs/H5–COFs/MCH/MB, vi: GCE/MXene–AuNPs/H5–COFs/MCH/MB/H2/Pb^{2+}, the higher right inset was Randles equivalent circuit for EIS. (c) DPV signals obtained by modifying electrodes by AuNPs and MXene–AuNPs, respectively. (d) DPV signals of the sensor with spherical COFs and urchin-shaped COFs as MB carriers, respectively. (e) Nitrogen adsorption–desorption isotherms of urchin-shaped COFs and spherical COFs before and after loading with MB. (f) Polyacrylamide gel electrophoresis image of the EDC cycle. (g) The fluorescence spectra and (h) DPV curves in the presence and absence of miRNA-21. Z_w: warburg impedance; R_s: solution resistance; R_{ct}: charge transfer resistance; C: capacitance; Z': real impedance; Z'': imaginary impedance; P: equilibrium pressure; P_0: saturation vapor pressure; BET: Brunauer–Emmett–Teller.

MB onto H5, the double-stranded DNA formed by the H5 stem-loop structure engaged in strong π–π stacking interactions with MB, thereby intercalating into the grooves of the DNA double helix and enhancing the current response [50]. Notably, when MB was loaded onto the H5–COFs modified electrode, a strong synergistic effect was observed. The porous channels of the COFs served as efficient loading sites, and the duplex structure of H5 further enhanced MB enrichment. As a result, the DPV signal was markedly amplified, indicating the potential of this platform for sensitive electrochemical sensing.

The effectiveness of multiple amplification strategy in sensor was systematically validated. Firstly, the enhancement effect of MXene–AuNPs on electrode performance was investigated. As shown in Fig. 4(c), the DPV signal of the electrode modified with MXene–AuNPs was 1.40 times stronger than that only modified with AuNPs. The large surface area of MXene provided additional attachment sites for the probe to improve electrode conductivity and achieve preliminary signal amplification.

Next, we evaluated the loading capacity of COFs, which serve as carriers for the signal molecule MB. Since acetic acid concentration during synthesis affects COFs morphology, we prepared regular spherical COFs for comparison with the urchin-shaped COFs (Fig. S6 in Appendix A). Fig. 4(d) illustrates the DVP responses of sensor employing these two COFs as MB carriers respectively. Result demonstrated that signal probe constructed from urchin-shaped COFs exhibited markedly superior DVP signals compared to spherical COFs. To further investigate the underlying mechanism, nitrogen adsorption–desorption isotherm at 77 K was employed to determine the surface areas of COFs with different morphologies before and after loading MB (Fig. 4(e)). Based on

the Brunauer–Emmett–Teller (BET) model, the surface area of the urchin-shaped COFs was calculated to be 1502.8 $m^2 \cdot g^{-1}$, significantly higher than that of the spherical COFs (899.79 $m^2 \cdot g^{-1}$). Following loading with MB, the area of the urchin-shaped COFs markedly decreased to 1015.9 $m^2 \cdot g^{-1}$, whereas that of the spherical COFs only slightly decreased to 871.28 $m^2 \cdot g^{-1}$. This obvious distinction revealed that MB molecules could fully loaded within the pore channels and micropore framework of the urchin-shaped COFs. By occupying the accessible pore volume, MB restricted the penetration of N_2 during adsorption measurements, which in turn led to a noticeable reduction in the measured surface area [51]. Pore size distribution analysis in Fig. S7 in Appendix A further showed that the urchin-shaped COFs exhibited a hierarchical structure combining both micropores and mesopores, with an average pore size of 3.28 nm, closely matching the theoretical calculations. Following MB loading, the average pore size decreased to 3.04 nm, a reduction comparable to the dimensions of MB (approximately 14.5 Å × 9.5 Å × 4.2 Å), directly demonstrating that MB molecules had entered the internal channels [43]. Collectively, these findings demonstrated that the unique hierarchical porous structure of the urchin-shaped COFs not only exhibited powerful molecular loading capacity but also effectively maintained the stable embedding of molecules. This provided a robust structural foundation for efficient electrochemical signal transmission within dual-mode sensor, thereby enabling further amplification of sensor signal.

Finally, the feasibility of EDC signal amplification was validated through native polyacrylamide gel electrophoresis (PAGE). Fig. 4(f) reveals that single-stranded DNA H1 (lane 1), H2 (lane 2), and H3 (lane 3) each produced sharp, well-defined bands at their expected positions. In contrast, when H1, H2, and H3 were mixed in equimolar amounts, lane 4 displayed a bright band with slower migration, clearly indicating the successful assembly of a stable H1–H2–H3 three-strand complex. Upon introduction of the auxiliary strand H4, a weaker new band corresponding to the H1–H4 duplex appeared, while the strong band of the triplex complex remained unchanged, suggesting that only a small fraction of H1 was sequestered by H4. With the introduction of a small amount of target miRNA-21, lane 6 exhibited significant alterations. Specifically, the triplex band disappeared completely, replaced by a dominant H1–H4 duplex band, and the intensity of the H2 band significantly increased. This marked change demonstrated that even extremely low concentrations of the target could effectively trigger the upstream EDC cycle, rapidly releasing large quantities of free H2 to sufficiently fuel the downstream DNAzyme reaction [52]. In summary, we developed a multi-amplification strategy for highly sensitive miRNA-21 detection. The design applied MXene–AuNPs to enhance probe loading and conductivity, urchin-shaped COFs to maximize signal molecule enrichment, and an EDC-driven DNAzyme cascade for robust signal amplification.

Building on this signal amplification strategy, DPV and fluorescence signals jointly evaluated the practical application efficacy of this dual-mode sensor for miRNA-21 detection. As depicted in Fig. 4(g), the presence of miRNA-21 initiated an EDC-driven cyclic amplification, which released large amounts of H2 to activate the downstream DNAzyme reaction. Under the action of Pb^{2+}, the substrate strand H5 was cleaved at the rA site, causing substantial release of H5–COFs probe from the electrode. Owing to the intrinsic fluorescence of COFs, these detached probes were readily collected and produced the strong fluorescence response. At the same time, DNAzyme-mediated cleavage reduced the number of MB-loaded probes retained on the electrode surface and thereby leading to a marked decrease in DPV signal (Fig. 4(h)). These results clearly demonstrated that the dual-mode sensor provided efficient and sensitive detection of miRNA-21, while the complementary and self-correcting features of the electrochemical and fluorescence signals effectively minimized false positives and substantially enhanced detection reliability.

3.5. Optimization of experimental conditions

To ensure the optimum performance of the dual-mode sensor in miRNA-21 detection, nine key experimental parameters were systematically optimized. Fig. 5(a) indicates that the ideal concentration of COFs was 1.00 $mg \cdot mL^{-1}$, which provided sufficient coupling with H5 and ensured probe stability. The ratio of H1:H2:H3 at 1:1.25:1.25 produced the most stable ternary complex (H1–H2–H3), significantly enhancing EDC amplification efficiency (Fig. 5(b)). Moreover, the cofactor H4 was found to be fully sufficient for cyclic amplification at 450 $pmol \cdot L^{-1}$. Lower concentrations resulted in insufficient amplification, while higher concentrations readily induced non-specific side reactions, diminishing the selectivity of detection (Fig. 5(c)). As shown in Fig. 5(d), 1.0 $mg \cdot mL^{-1}$ of MXene–AuNPs achieved a uniform surface distribution and facilitated faster electron transfer, thereby reducing interfacial resistance at the electrode interface. Simultaneously, the optimal concentration of Pb^{2+} was illustrated in Fig. 5(e), and 20 $mmol \cdot L^{-1}$ Pb^{2+} ensured efficient substrate cleavage and stronger signal output. As the key sensing module, the influence of COFs on fluorescence signals under different solvent conditions was first investigated (Fig. 5(f)). Ethanol at a concentration of 50% was demonstrated to significantly enhance the luminescence intensity of the COFs. This was resulted from ethanol molecules modulating the microenvironment of the COFs, reducing non-radiative energy loss and avoiding fluorescence quenching effects caused by excessive solvent polarity. For electrochemical signal, 2 $mmol \cdot L^{-1}$ of MB was identified as the optimal loading concentration. This moderate concentration ensured efficient MB enrichment within the H5–COFs structure while avoiding excessive accumulation that could cause signal quenching or reduced conductivity (Fig. 5(g)). Finally, in reaction kinetics, the optimal catalysis time for the DNAzyme was determined to be 90 min, allowing for complete cleavage without introducing background signal accumulation (Fig. 5(h)). Simultaneously, the optimal incubation time for MB with urchin-shaped COFs was established at 75 min. This duration ensured sufficient MB enrichment within the pore structure while effectively preventing non-specific adsorption caused by prolonged incubation (Fig. 5(i)). Under these optimized conditions, each signal pathway was significantly enhanced. More importantly, the electrochemical and fluorescence channels worked synergistically, delivering high sensitivity, excellent specificity, and reliable performance. Detailed optimization procedures are provided in Section S1.3 in Appendix A.

3.6. The analytical performance of dual-mode sensor

Under the optimized experimental conditions, the performance of the dual-mode sensor was evaluated by detecting varying concentrations of miRNA-21. As illustrated in Fig. 6(a), the electrochemical current decreased with increasing miRNA-21 concentration. This trend aligns with the proposed mechanism that higher miRNA-21 levels trigger more EDC-driven cycles, releasing additional H2 strands. These H2 strands then promote cleavage of the H5 substrate, reducing the amount of MB-loaded probes retained on the electrode surface and consequently diminishing the DPV signal. Quantitative analysis revealed a strong linear relationship between DPV current and the logarithm of miRNA-21 concentration from 1 to 10^5 $fmol \cdot L^{-1}$, with a regression equation of $I = -1.39 \lg C_{miRNA\text{-}21} + 10.32$ ($R^2 = 0.997$) and the detection limit (LOD) of 0.285 $fmol \cdot L^{-1}$ (Fig. 6(b)). Similarly, in fluorescence mode, higher concentrations of miRNA-21 led to greater release of H5–COFs probe, yielding enhanced fluorescence signal in 50% ethanol

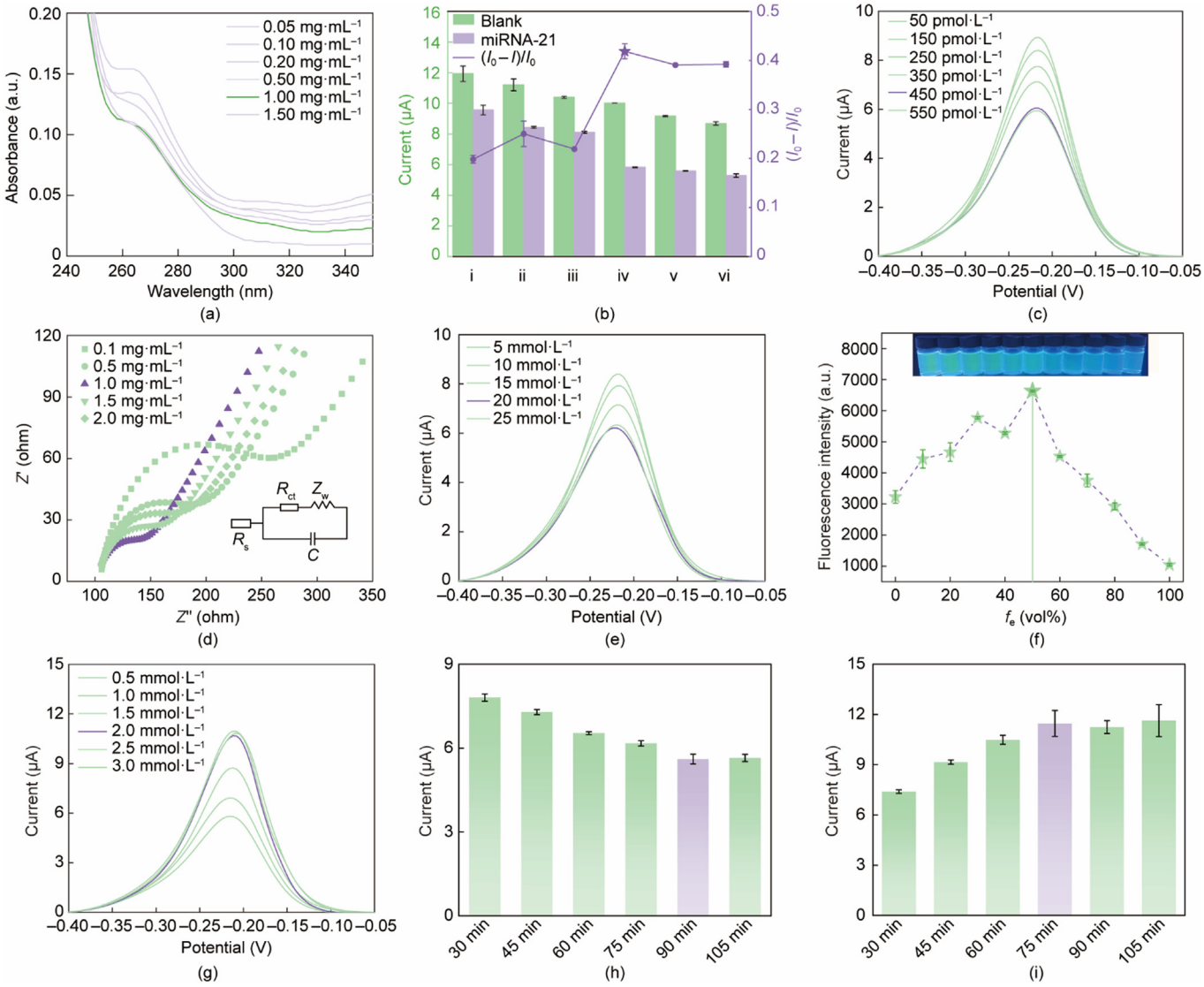


Fig. 5. Optimization of experimental conditions for dual-mode sensor. The parameters optimized were (a) the coupling concentration of the urchin-shaped COFs and (b) the molar ratio of H1, H2, and H3, in which curves i–vi correspond to H1:H2:H3 ratios of 1:0.5:0.5, 1:0.75:0.75, 1:1:1, 1:1.25:1.25, 1:1.5:1.5, and 1:1.75:1.75, respectively. (c) The concentration of the fuel strand H4. (d) The concentration of MXene–AuNPs modified onto the GCE. (e) The concentration of Pb^{2+}. (f) Ethanol concentration. (g) The loading amount of MB. (h) The reaction time of DNAzyme. (i) MB–COFs incubation time. I_0: initial fluorescence intensity; I: fluorescence intensity; f_e: volume fraction of ethanol.

solution (Fig. 6(c)). Furthermore, as demonstrated in Fig. S8 in Appendix A, under ultraviolet illumination, the fluorescence intensity of this sensor exhibited a marked increase with rising concentrations of miRNA-21, clearly reflecting its outstanding concentration dependence. Quantitative analysis revealed that the fluorescence intensity also displayed a robust linear dependence on the logarithm of miRNA-21 concentration within the range of 1–10^5 fmol·L^{-1} (Fig. 6(d)). The calibration equation was F = 449.66lg$C_{\text{miRNA-21}}$ + 966.51 (R^2 = 0.997), with the LOD of 0.342 fmol·L^{-1}. The electrochemical mode demonstrated slightly higher sensitivity than the fluorescence mode, likely due to the greater precision of electron transfer compared with fluorescence processes. Notably, compared to other sensors, this dual-mode platform showed superior sensitivity in the detection of miRNA-21 (Table S2 in Appendix A). Such performance enhancement can be attributed primarily to the synergistic effects of the highly conductive MXene–AuNPs interface, the high loading capacity of the urchin-shaped COFs, and the cascade amplification strategy. Notably, the synergistic effect of this platform follows a stepwise mechanism, with each functional module promoting subsequent signal amplification and transduction. The MXene–AuNPs interface enhanced electron transfer efficiency and provided a foundation for the high-density assembly of urchin-shaped COFs, thereby maximizing probe loading capacity. This structural advantage further amplifies the efficiency of the EDC-driven cyclic cleavage reaction, enabling the miRNA-21-triggered sensing process to significantly reduce probe density at the electrode interface while simultaneously increasing the release of fluorescent probes into solution. Consequently, pronounced variations in both electrochemical and fluorescence signals were generated. Importantly, the two signal modes move in opposite directions yet remain mechanistically coupled. This opposing correlation provides the system with intrinsic self-calibration, significantly improving the reliability and robustness of the analytical performance.

We evaluated the specificity of the dual-mode sensor by introducing several potential interferents including let-7a, miRNA-155, single-base mismatched miRNA-21 (smRNA), and double-base mismatched miRNA-21 (tmRNA). As shown in Fig. 7(a), the sensor

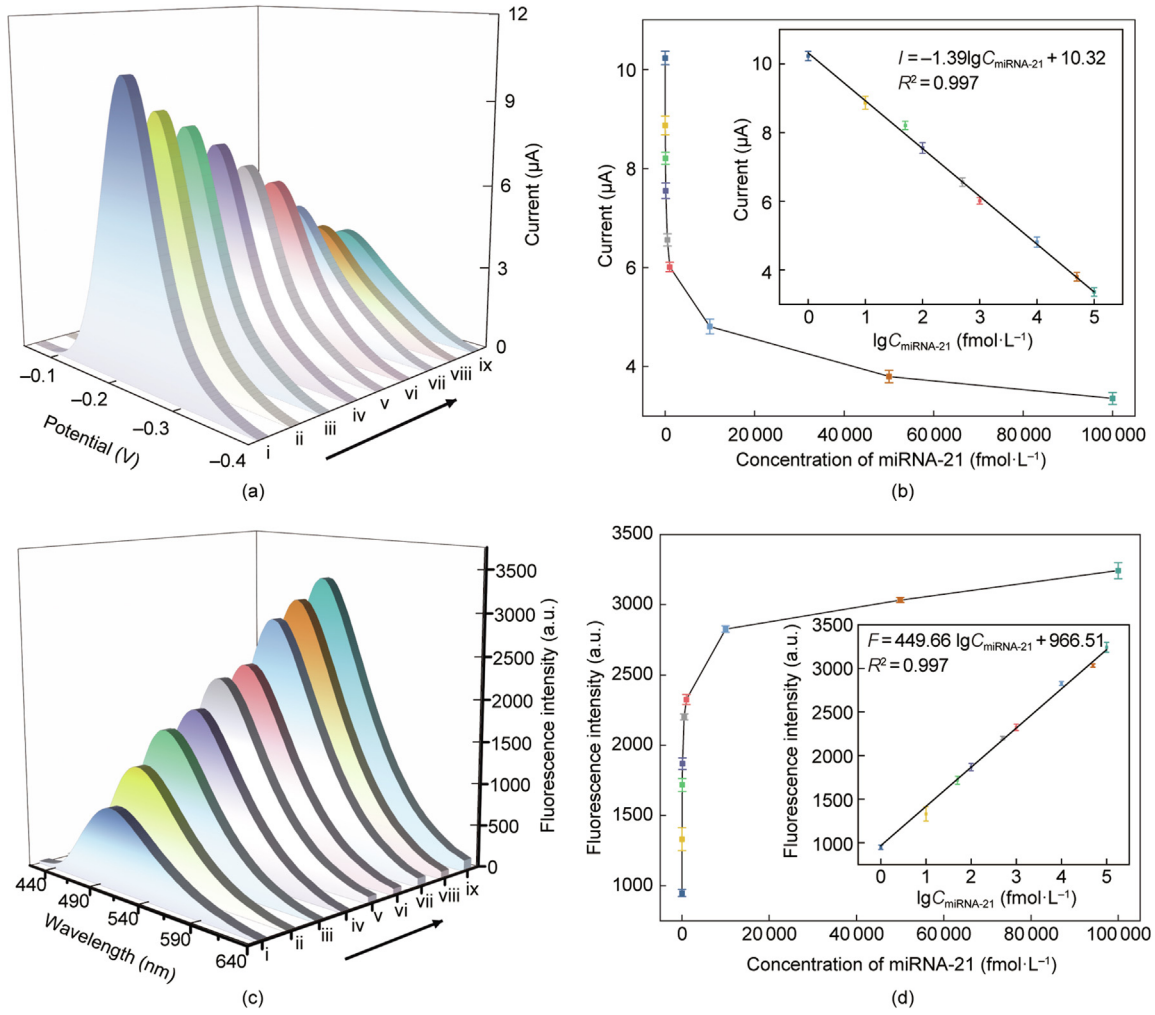


Fig. 6. (a) DPV response curves for miRNA-21 at different concentrations (i–ix: 1, 10, 50, 100, 500, 1 000, 10 000, 50 000, and 100 000 fmol·L^{-1}) using the electrochemical detection mode. (b) Corresponding calibration curve derived from (a). The error bars represent the standard deviations of repeated measurements from six experiments. (c) Fluorescence spectra for miRNA-21 at different concentrations (i–ix: 1, 10, 50, 100, 500, 1 000, 10 000, 50 000, and 100 000 fmol·L^{-1}) using the fluorescence detection mode. (d) Corresponding calibration curve derived from (c). The error bars represent the standard deviations of repeated measurements from six experiments.

presented a pronounced electrochemical decrease and the fluorescence enhancement only in response to miRNA-21, while interference from the other sequences was negligible. More importantly, in mixed solutions containing both interferents and miRNA-21, the sensor response closely matched that observed with miRNA-21 alone. These results confirmed its high selectivity and strong anti-interference capability. Furthermore, to evaluate the reproducibility of this dual-mode sensor, electrochemical detection was conducted on nine electrodes prepared under identical conditions, with the collected solutions subsequently subjected to fluorescence analysis. As shown in Fig. 7(b), the electrochemical signals displayed minimal variation, with a relative standard deviation (RSD) of 1.40%. Similarly, the fluorescence signals were equally consistent, with an RSD of 0.87%, fully demonstrating the excellent repeatability of this platform. To examine storage stability, the DPV and fluorescence intensity were measured after storage at 4 °C for 0, 12, 24, 36, and 48 h. Even after 48 h, the electrochemical response retained 94.98% of its initial value, while the fluorescence intensity maintained 98.22% of its baseline benefiting from the intrinsic stability of the COFs (Fig. 7(c)). These results highlighted the stability of the dual-mode sensor under storage conditions, indicating its potential for long-term use in complex body fluid samples.

3.7. Real sample analysis

Before real sample analysis, the pH stability of the sensor was evaluated to ensure reliable performance in biological samples such as serum and cancer cell. miRNA-21 standard solutions (1000 fmol·L^{-1}) with pH values ranging from 6.0 to 8.0 were tested under identical conditions. Fig. S9 in Appendix A indicates that pH variations within the physiologically relevant range have negligible effects on both electrochemical and fluorescence responses. Subsequently, to evaluate the practical applicability of the dual-mode sensor, recovery tests were conducted by spiking varying concentrations of miRNA-21 into serum diluted twenty-fold (Table 1). In the electrochemical mode, recovery rates ranged from 102.13% to 104.58% with low RSDs of 1.37%–4.89%. Similarly, the fluorescence mode delivered satisfactory recovery rates of 105.96%–108.96%, with all RSDs below 5%. These findings indicated that the sensor could achieve accurate and reliable detection of miRNA-21 even in complex matrices. Beyond simulated samples, we further examined its applicability in real biological systems. The levels of miRNA-21 were measured in cervical cancer cells (HeLa), breast cancer cells (MCF-7), and colorectal cancer cells (HCT116) using the dual-mode sensor, with comparison to qRT-PCR. As shown in Fig. 7(d), the detection results under electrochemical

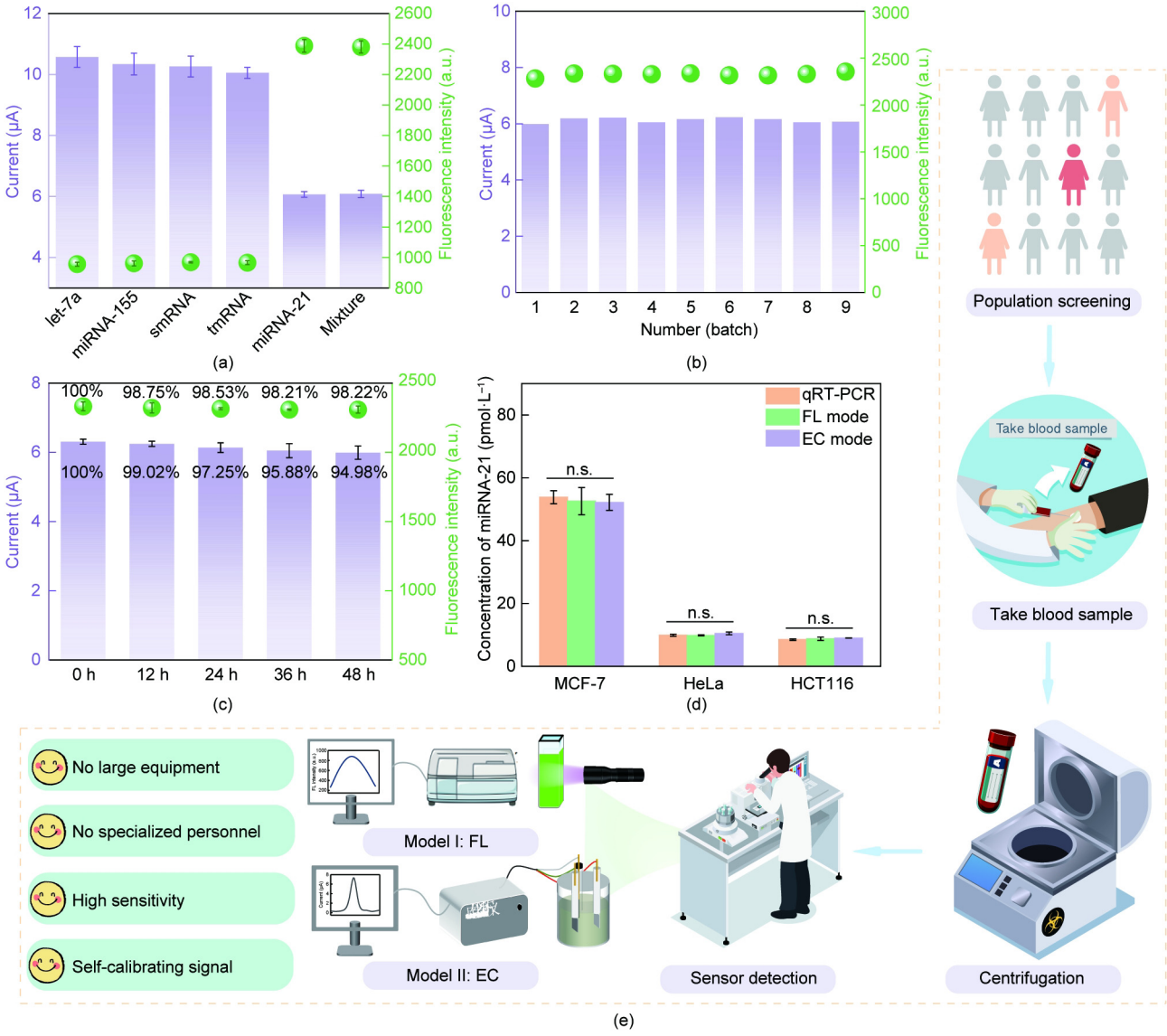


Fig. 7. Performance analysis of dual-modes sensors. (a) Specificity of the dual-modes sensor strategy towards different miRNAs. The error bars represent the standard deviations of repeated measurements from six experiments. (b) Repeatability assessment for different electrodes. (c) Stability analysis over 48 h storage. The error bars represent the standard deviations of repeated measurements from six experiments. (d) Comparison of the determination of miRNA-21 concentrations in MCF-7, HeLa, and HCT116 cells using the proposed dual-mode sensor and the conventional qRT-PCR method. Statistical analysis was performed using one-way repeated-measures analysis of variance (ANOVA) to compare measurements obtained by different detection modes within the same cell line. (e) Process diagram for the application of dual-mode sensors in early cancer screening. n.s.: not significant.

Table 1
The detection of miRNA-21 in human serum samples.

Sample	Detected (fmol·L^{-1})	Added (fmol·L^{-1})	Found (fmol·L^{-1})	RSD (n = 6)	Recovery
Electrochemical mode	Not detected				
1		100	104.33	4.89%	104.33%
2		1 000	1 045.82	1.37%	104.58%
3		10 000	10 212.56	4.59%	102.13%
Fluorescent mode	Not detected				
1		100	106.29	4.88%	106.29%
2		1 000	1059.60	3.71%	105.96%
3		10 000	10 895.58	4.96%	108.96%

and fluorescence modes were highly consistent. miRNA-21 expression was highest in breast cancer cells, followed by cervical cancer, and lowest in colorectal cancer. This trend closely aligned with previously reported expression patterns and matched the qRT-PCR results [53,54]. The results conclusively demonstrated the reliable performance of the fluorescence–electrochemical dual-mode sensor for miRNA-21 in clinical samples. Notably, the platform requires no large-scale instrumentation or specialized training.

The multi-signal amplification strategy provides high sensitivity, while the self-calibrating dual-output feature minimizes the risk of false positives associated with low miRNA-21 abundance. These advantages position the sensor as a promising tool for clinical diagnostics and early disease screening (Fig. 7(e)).

4. Conclusions

In this study, we developed a multiple amplified dual-mode sensor based on urchin-shaped COFs for the ultrasensitive detection of cancer biomarker miRNA-21. Benefiting from the large surface area and superior conductivity of the MXene–AuNPs, the electrochemical response was significantly enhanced, achieving approximately 1.4 times increase compared to AuNPs alone. The unique hierarchical porous structure of the urchin-shaped COFs facilitated more efficient MB loading, providing a robust structural basis for signal amplification. Furthermore, the low-cost, enzyme-free EDC–DNAzyme cascade amplification strategy activated by miRNA-21 markedly boosted the sensitivity of the dual-mode sensor. Importantly, the urchin-shaped COFs served simultaneously as fluorescent element and carrier, enabling the sensor with dual-mode analysis capabilities to effectively correct systematic errors and achieve signal self-calibration.

With these synergistic advantages, the sensor achieved detection limits of 0.285 fmol·L^{-1} in electrochemical mode and 0.342 fmol·L^{-1} in fluorescence mode. It also demonstrated excellent selectivity, repeatability, and stability. In complex samples, its performance closely matched qRT-PCR results, highlighting strong potential for bioanalysis.

Building upon these results, future efforts may focus on optimizing the stability of the sensing platform in complex biological samples. In addition, extending this strategy to enable simultaneous detection of multiple miRNAs and integration with portable devices holds promise for real-time and point-of-care monitoring. Such developments will further promote the translation of this non-invasive sensing approach into clinical practice and broaden its applicability to other low-abundance disease-related biomarkers.

CRediT authorship contribution statement

Xinxue Zhang: Writing – review & editing, Writing – original draft, Formal analysis, Data curation, Conceptualization. **Pengfei Dong:** Writing – review & editing, Visualization, Validation. **Youfa Wang:** Writing – review & editing, Visualization, Validation. **Shuang Wu:** Writing – review & editing, Visualization, Validation. **Lili Zhang:** Writing – review & editing, Visualization, Validation. **Jie Han:** Writing – review & editing, Visualization, Validation. **Geoffrey I. N. Waterhouse:** Writing – review & editing. **Quancai Sun:** Writing – review & editing. **Jing Huang:** Writing – original draft. **Jin Wang:** Writing – review & editing, Supervision, Resources, Project administration, Funding acquisition, Conceptualization.

Declaration of competing interest

The authors declare that they have no known competing financial interests or personal relationships that could have appeared to influence the work reported in this paper.

Acknowledgments

We are grateful for the financial support from the Basic Research Program of Jiangsu (BK20250072), the Fundamental Research Funds for the Central Universities, Postgraduate Research & Practice Innovation Program of Jiangsu Province (KYCX25_0534), and the Southeast University Innovation Capability Enhancement Plan for Doctoral Students (CXJH_SEU 26225).

Appendix A. Supplementary data

Supplementary data to this article can be found online at https://doi.org/10.1016/j.eng.2026.03.007.

References

[1] Negahdary M, Angnes L. Application of electrochemical biosensors for the detection of microRNAs (miRNAs) related to cancer. Coord Chem Rev 2022;464:214565.
[2] Preethi KA, Selvakumar SC, Ross K, Jayaraman S, Tusubira D, Sekar D. Liquid biopsy: exosomal microRNAs as novel diagnostic and prognostic biomarkers in cancer. Mol Cancer 2022;21(1):54.
[3] Chen M, Choi HK, Goldston LL, Hou Y, Jiang C, Lee KB. Advanced cancer liquid biopsy platform for miRNA detection in extracellular vesicles using CRISPR/Cas13a and gold nanoarrays. ACS Nano 2025;19(35):31438–56.
[4] Zhao H, Yan Y, Zhang L, Li X, Jia L, Ma L, et al. DNA molecular computing with weighted signal amplification for cancer miRNA biomarker diagnostics. Adv Sci 2025;12(22):e2416490.
[5] Dong JX, Zhang SM, Li YL, Zhang X, Fan YJ, Su M, et al. Photocontrollable DNA walker-based molecular circuit for the tunable detection of microRNA-21 using metal–organic frameworks as label-free fluorescence tags. Anal Chem 2023;95(45):16744–53.
[6] Yang X, Yu C, Yang B, Jiang C, Gao R, Li W, et al. DNA-enabled self-resetting electrochemical sensor for microRNA detection. Small Methods 2025;9(6):e2402095.
[7] Tang D, Shi J, Wu Y, Luo H, Yan J, Huang KJ, et al. Flexible self-powered sensing system based on novel DNA circuit strategy and graphdiyne for thalassemia gene by rapid naked-eye tracking and open-circuit voltage. Anal Chem 2023;95(44):16374–82.
[8] Du S, Xie B, Gao H, Zhang J, Fu H, Liao F, et al. Self-powered DNAzyme walker enables dual-mode biosensor construction for electrochemiluminescence and electrochemical detection of microRNA. Anal Chem 2023;95(17):7006–13.
[9] Hou YY, Xu J, Wang FT, Dong Z, Tan X, Huang KJ, et al. Construction of an integrated device of a self-powered biosensor and matching capacitor based on graphdiyne and multiple signal amplification: ultrasensitive method for microRNA detection. Anal Chem 2021;93(46):15225–30.
[10] Shi J, Liu S, Li P, Lin Y, Luo H, Wu Y, et al. Self-powered dual-mode sensing strategy based on graphdiyne and DNA nanoring for sensitive detection of tumor biomarker. Biosens Bioelectron 2023;237:115557.
[11] Xu J, Liu Y, Huang KJ, Hou YY, Sun X, Li J. Real-time biosensor platform based on novel sandwich graphdiyne for ultrasensitive detection of tumor marker. Anal Chem 2022;94(49):16980–6.
[12] Wang FT, Hou YY, Tan X, Huang KJ, Xu J, Cai R. Real-time multiple signal amplification self-powered biosensing platform for ultrasensitive detection of microRNA. Biosens Bioelectron 2023;222:114933.
[13] Li Y, Luo Z, Zhang C, Sun R, Zhou C, Sun C. Entropy driven circuit as an emerging molecular tool for biological sensing: a review. Trends Analyt Chem 2021;134:116142.
[14] Cheng W, Pan H, Chen J, He M, Wang Z, Xiang Y. Enzyme-free and triple sensitivity amplification for electrochemical detection of exosomal microRNA. Anal Chem 2025;97(9):5244–50.
[15] Tian L, Zhang J, Zhang Y, Oderinde O, Li C, Duan L, et al. Bipedal DNAzyme walker triggered dual-amplification electrochemical platform for ultrasensitive ratiometric biosensing of microRNA-21. Biosens Bioelectron 2023;220:114879.
[16] Sun Y, Peng Y, Sun Y, Xu D. An enzyme-free and label-free multiplex detection of miRNAs by entropy-driven circuit coupled with capillary electrophoresis. Talanta 2025;281:126850.
[17] Shuai HL, Huang KJ, Chen YX, Fang LX, Jia MP. Au nanoparticles/hollow molybdenum disulfide microcubes based biosensor for microRNA-21 detection coupled with duplex-specific nuclease and enzyme signal amplification. Biosens Bioelectron 2017;89(Pt 2):989–97.
[18] Huang KJ, Liu YJ, Wang HB, Wang YY, Liu YM. Sub-femtomolar DNA detection based on layered molybdenum disulfide/multi-walled carbon nanotube composites, Au nanoparticle and enzyme multiple signal amplification. Biosens Bioelectron 2014;55:195–202.
[19] Fan Z, Zhao X, Dong Y, Zhou J, Li Y, Wang J, et al. Protein-free, ultrasensitive miRNA analysis based on an entropy-driven catalytic reaction switched on a smart-responsive DNAzyme dual-walker amplification strategy. Int J Biol Macromol 2022;223(Pt A):931–8.
[20] Huang Q, Wang K, Wang Y. Highly sensitive miRNA-21 detection with enzyme-free cascade amplification biosensor. Talanta 2024;273:125928.
[21] Yao Y, Long C, Gao Z, Cheng Y, Chen S, Liu Q, et al. Magnetic three-dimensional ordered DNA arrays for colorimetric detection of dual-miRNAs based on molecular logic gate. Sens Actuators B Chem 2025;445:138545.
[22] Zhang X, Wang Y, Wu S, Han J, Raghavan V, Wang J. Portable sensor devices based on multifunctional framework materials: recent advances for food

safety assurance by on-site detection. Trends Food Sci Technol 2025;159:104965.
[23] Khan M, Sun X, Attique F, Saleh MT, Ahmad N, Atiq K, et al. Unveiling the future: breakthroughs and innovations in MXene-based electrochemical sensors. Chem Eng J 2025;207:160392.
[24] Zhang J, Jin H, Suo Z, Shen H, Chen X, Liu Y, et al. Highly conductive MXene–AuNPs and high current AuPd NPs/UiO-66 electrochemical sensor combining multiple signal amplification strategies for tetracycline detection. Chem Eng J 2025;504:158980.
[25] Guo H, Zhang W, He L, Fu Y, Li W, Chen M. Accordion-shaped MXene/PANI-Pd loaded with dual aptamer rolling circle-amplified 3D DNA networks for enhanced sensitivity in circulating tumor cell detection. Biosens Bioelectron 2025;287:117723.
[26] Mohammadniaei M, Koyappayil A, Sun Y, Min J, Lee MH. Gold nanoparticle/MXene for multiple and sensitive detection of oncomiRs based on synergetic signal amplification. Biosens Bioelectron 2020;159:112208.
[27] Meng Z, Mirica KA. Covalent organic frameworks as multifunctional materials for chemical detection. Chem Soc Rev 2021;50(24):13498–558.
[28] Li Z, Luo Z, Liu J, Bao T, Wu Z, Wen W, et al. Magnetic beads-assisted split DNAzyme cleavage-driven assembly of functionalized covalent organic frameworks for highly sensitive electrochemical detection of microRNA. Sens Actuators B Chem 2024;409:135594.
[29] He J, Zhang D, Liu H, Sun B. A turn-on fluorescence molecularly imprinted sensor based on covalent organic framework for specific and visual detection of α-dicarbonyl compounds. Sens Actuators B Chem 2024;404:135253.
[30] Song X, Gao H, Yuan R, Xiang Y. Trimetallic nanoparticle-decorated MXene nanosheets for catalytic electrochemical detection of carcinoembryonic antigen via Exo III-aided dual recycling amplifications. Sens Actuators B Chem 2022;359:131617.
[31] Song D, Jiang X, Li Y, Lu X, Luan S, Wang Y, et al. Metal-organic frameworks-derived MnO_2/Mn_3O_4 microcuboids with hierarchically ordered nanosheets and Ti_3C_2 MXene/Au NPs composites for electrochemical pesticide detection. J Hazard Mater 2019;373:367–76.
[32] Ali M, Hasan E, Barman SC, Hedhili MN, Alshareef HN, Alsulaiman D. Peptide nucleic acid-clicked $Ti_3C_2T_x$ MXene for ultrasensitive enzyme-free electrochemical detection of microRNA biomarkers. Mater Horiz 2024;11(20):5045–57.
[33] Chen Z, Wu C, Yuan Y, Xie Z, Li T, Huang H, et al. CRISPR–Cas13a-powered electrochemical biosensor for the detection of the *L452R* mutation in clinical samples of SARS-CoV-2 variants. J Nanobiotechnology 2023;21(1):141.
[34] Liu F, Han L, Yang Y, Xue Z, Lu X, Liu X. Designable synthesis of a novel layered MXene loaded gold nanocluster composite for efficient electrochemical sensing of homocysteine in biological samples. Chem Eng J 2023;461:141928.
[35] Zheng Z, Wu W, Yang T, Wang E, Du Z, Hou X, et al. *In situ* reduced MXene/AuNPs composite toward enhanced charging/discharging and specific capacitance. J Adv Ceram 2021;10(5):1061–71.
[36] Ma W, Zheng Q, He Y, Li G, Guo W, Lin Z, et al. Size-controllable synthesis of uniform spherical covalent organic frameworks at room temperature for highly efficient and selective enrichment of hydrophobic peptides. J Am Chem Soc 2019;141(45):18271–7.
[37] Yan W, Zhang J, Wang C, Xia Y. An urchin-shaped covalent organic framework with rich nitrogen for efficient removal of neonicotinoid insecticides in honey and fruits. Food Chem 2023;429:136872.
[38] Tian Y, Mou Y, Zhang W, Sun Z, Yin Y, Han L, et al. A fluorescence and colorimetric dual-mode aptasensor for kanamycin detection. Biosens Bioelectron 2025;268:116911.
[39] Guo H, Ma P, Dong X, Qin M, Zhang Y, Wang Z. CRISPR/Cas12a-mediated fluorescent aptasensor based on DNA walker amplification for oxytetracycline detection. Biosens Bioelectron 2025;271:117031.
[40] Wei S, Wang F, Zhang L, Zhao C, Li J, Wang J. A portable smartphone-assisted highly emissive magnetic covalent organic framework-based fluorescence sensor for the detection of *Salmonella typhimurium*. Sens Actuators B Chem 2023;392:134076.
[41] Ming P, Lai H, Liu Y, Wang J, You F, Sun D, et al. Aptasensor development for T-2 toxin detection utilizing a dual signal amplification strategy: synergistic effects of bimetallic oxide $(Ce–In)O_x$ and $COF_{TAPB\text{-}DMTP}$. Sens Actuators B Chem 2023;396:134602.
[42] Li Z, Wang Y, Pellei M, Zhang S, Wang M, Gabrielli S, et al. Trinuclear copper cluster-based COF with a high content of $Cu–N_2$ single-atom sites: a multivariate signal-amplified photoelectrochemical aptasensor for the sensitive detection of mycotoxins. Chem Eng J 2025;505:159603.
[43] Wen SH, Zhang H, Yu S, Ma J, Zhu JJ, Zhou Y. Nanozyme coating-gated multifunctional COF composite based dual-ratio enhanced dual-mode sensor for highly sensitive and reliable detection of organophosphorus pesticides in real samples. J Hazard Mater 2024;480:135791.
[44] Bai Y, Gao W, Wei J, Yu B, Zhang L, Zhu P, et al. Biomimetic cascade intelligent paper chip sensor based on bimetallic porphyrin-based covalent organic framework with triple-enzyme mimetic activities. Chem Eng J 2024;490:151628.
[45] Gao M, Fu Q, Wang M, Zhang K, Zeng J, Wang L, et al. Facile synthesis of porous covalent organic frameworks for the effective extraction of nitroaromatic compounds from water samples. Anal Chim Acta 2019;1084:21–32.
[46] Zang L, He M, Wu Z, Chen B, Hu B. Imine-linked covalent organic frameworks coated stir bar sorptive extraction of non-steroidal anti-inflammatory drugs from environmental water followed by high performance liquid chromatography-ultraviolet detection. J Chromatogr A 2021;1659:462647.
[47] Qiu G, Wang Y, Zhang W, Bao T, Wu Z, Zhang X, et al. Multispatially localized DNA walker coupling covalent organic framework for dual-mode detection of nucleocapsid protein using the walking–recycling–conversion strategy. Anal Chem 2024;96(46):18464–73.
[48] Wang H, He B, Yang J, Liu Y, Liang Y, Wang J, et al. An ultra-sensitive electrochemical aptasensor detection for di(2-ethylhexyl) phthalate based a cleavage effect of Mg^{2+}-driven bipedal DNA walker motor. Sens Actuators B Chem 2024;406:135412.
[49] Schmuck JF, Borggräfe J, Etzkorn M. The dynamic world of the 8–17 DNAzyme. Nat Commun 2024;15(1):5145.
[50] Jia F, Liu D, Dong N, Li Y, Meng S, You T. Interaction between the functionalized probes: the depressed efficiency of dual-amplification strategy on ratiometric electrochemical aptasensor for aflatoxin B1. Biosens Bioelectron 2021;182:113169.
[51] Yu M, Dong H, Zheng Y, Liu W. Ternary metal oxide embedded carbon derived from metal organic frameworks for adsorption of methylene blue and acid red 73. Chemosphere 2021;280:130567.
[52] Lv Y, Sun Y, Zhou Y, Khan IM, Niazi S, Yue L, et al. Cascade DNA circuits mediated CRISPR–Cas12a fluorescent aptasensor based on multifunctional Fe_3O_4@hollow-TiO_2@MoS_2 nanochains for tetracycline determination. Small 2023;19(16):e2206105.
[53] Zhao W, Zhang X, Tian R, Li H, Zhong S, Yu R. The sensor platform combined with dual signal amplification and based on UCNPs and CRISPR/Cas12a for miRNA-21 detection. Sens Actuators B Chem 2023;393:134238.
[54] Pei J, Li L, Li C, Li Z, Wu Y, Kuang H, et al. Dumbbell probe-bridged CRISPR/Cas13a and nicking-mediated DNA cascade reaction for highly sensitive detection of colorectal cancer-related microRNAs. Biosens Bioelectron 2025;273:117190.